Iranian Journal of Medical Physics

ijmp.mums.ac.ir

# AI-Driven Identification of Microplastics via STIM-Based Proton Transmission: A Computational Proof-of-Concept

Marjan Atghae[1], Mohammad Reza Rezaie[2*], Hossein Afarideh [2], Ali Negarestani[1]

1. Department of Nuclear Engineering, Faculty of Sciences and Modern Technologies, Graduate University of Advanced Technology, Kerman, Iran
2. Department of Nuclear Engineering, Faculty of Physics and Energy Engineering, Amirkabir University of Technology, Tehran, Iran

**ARTICLE INFO**

***Article type:***
Original Paper

***Keywords:***
Microplastic
Scanning Ion Transmission Microscopy (STIM)
MIL-101(Cr) Nanofilter
MCNPX Simulation
Bi LSTM–Transformer
Neural Network

**ABSTRACT**

***Introduction:*** This simulation-driven study investigated the potential of a non-destructive detection system concept for microplastic (MP) pollution using a computational framework. Traditional detection methods are often time-consuming or lack the sensitivity required for real-time monitoring. We proposed an integrated approach combining proton Scanning Transmission Ion Microscopy (STIM) with Metal-Organic Framework (MOF) nanofilters and deep learning-based analysis.

***Material and Methods:*** Computational modeling was conducted using the Monte Carlo N-Particle extended (MCNPX) code to simulate proton beam interactions (at 30 and 60 MeV) with MPs. Polyimide was utilized as a simulation proxy for the MIL-101(Cr) MOF nanofilters to represent the structural density and elemental composition. The physical changes in the proton Bragg peak and energy loss spectra were analyzed. To automate the detection process, a sequential-attention architecture integrating Bidirectional Long Short-Term Memory (BiLSTM) and Transformer models was developed and trained on the simulated spectral data.

***Results:*** The simulation-derived results suggested that the integration of MOF nanofilters could enhance the sensitivity of STIM to minor density variations caused by microplastics within a controlled computational environment. The BiLSTM-Transformer model achieved high predictive accuracy on the simulated dataset, with an $R^2$ value of 0.982 and a Mean Absolute Error (MAE) of 0.015. Detailed statistical uncertainties (standard deviations) for the MCNPX outputs are reported in the Results section.

***Conclusion:*** This simulation study demonstrates the theoretical feasibility of using AI-enhanced proton STIM for the identification of microplastics. While the current findings are based on deterministic Monte Carlo outputs, the high accuracy of the BiLSTM-Transformer model provides a computational proof-of-concept. Future experimental work is required to bridge the gap between simulation and real-world cyclotron-based monitoring systems, particularly regarding electronic noise and detector efficiency.

► *Please cite this article as:*
Atghae M, Rezaie MR, Afarideh H, Negarestani A. AI-Driven Identification of Microplastics via STIM-Based Proton Transmission: A Computational Proof-of-Concept. Iran J Med Phys 2026; 23 (2): 76-85. 10.22038/ijmp.2026.95156.2685.

## Introduction

Microplastics, defined as plastic fragments smaller than 5 mm, have emerged as persistent environmental contaminants widely dispersed across aquatic, terrestrial, and atmospheric systems [1,2]. These particles originate from diverse sources, including packaging materials; synthetic textiles particularly fibers released during washing processes [3,4]; the degradation of commercial plastic bags [5]; and microbeads formerly used in cosmetic products [6]. Recent studies have confirmed the presence of microplastics even in highly regulated environments, with detections reported in tap water [7], rain and snow, as well as indoor air. Consequently, human exposure may occur continuously through inhalation, ingestion, and dermal contact [8]. Beyond their physical presence, microplastics pose a significant chemical risk due to their large specific surface area and strong adsorption capacity [9]. They can accumulate and transport hazardous substances, including heavy metals, chlorates, and persistent organic pollutants, which may contribute to cellular toxicity, endocrine disruption, immune suppression, and an increased risk of chronic diseases such as cancer [10,11]. Despite growing awareness, a major challenge in microplastic research remains the lack of rapid, cost-effective, and non-destructive detection techniques suitable for continuous or in-situ environmental monitoring [12,13]. Conventional analytical methods such as SEM-EDS, Raman spectroscopy, and FTIR are widely used [14]; however, they typically require extensive sample preparation and laboratory-based analysis, which limits their practicality for continuous or field-based monitoring of micro- and nanoplastics [15]. Therefore, beyond physical capture, there is a need for approaches that can potentially sense and identify microplastic contamination with minimal sample preprocessing and reduced dependence on laboratory workflows. In this context, metal–organic frameworks (MOFs) have attracted increasing

*Corresponding Author: Tel: +98-3432653340; Email: mohamadreza45@gmail.com

attention due to their uniform porous architecture, exceptionally high surface area, and tunable surface chemistry [16,17]. Among them, MIL-101(Cr), a chromium-based MOF featuring large pore diameters (~29 and ~34 Å) and high structural stability under moderate temperature and humidity conditions, has demonstrated strong potential for the adsorption and retention of micro- and nanoplastics [18]. Previous studies have shown that MIL-101 nanoparticles and nanofilters can effectively interact with polymeric particles through van der Waals forces, hydrogen bonding, and surface functionalization (e.g., amine or carboxyl groups), enabling selective affinity toward plastics such as PE, PP, and PET [19]. Advancements in MIL-101-based filtration technologies could therefore contribute to reducing long-term human exposure to plastic-associated pollutants while simultaneously improving air and water quality [20]. For computational tractability in the present Monte Carlo workflow, the MOF filtration layer is represented using a surrogate material with comparable stopping-power characteristics in the investigated energy range; the rationale for this proxy is provided in the Discussion. Scanning ion transmission microscopy (STIM) provides a complementary, physics-based approach [21] for indirect microplastic detection. In STIM, a focused monoenergetic proton beam traverses the sample in transmission mode, and the resulting energy loss is recorded with micrometer-scale depth sensitivity (approximately 10 µm in the present configuration) [22]. Unlike surface-sensitive techniques such as Rutherford backscattering spectrometry (RBS) [23], STIM can provide bulk density information, making it suitable for detecting embedded sub-micron inclusions. Key STIM observables including the Bragg peak position and height, transmission ratio, and dE/dx profiles can form a spectral fingerprint of density perturbations caused by microplastics. In this work, proton beam energies of 30 MeV (air) and 60 MeV (water) are investigated to extend STIM beyond its traditional low-energy regime (0.5–3 MeV) [24]. These higher energies are expected to enable transmission through millimeter-scale environmental samples while maintaining sensitivity to PMMA microplastics with thicknesses down to 0.5 µm. Monte Carlo N-Particle eXtended (MCNPX) simulations are used to model proton transport, energy deposition, scattering, and transmission [25,26] within the MIL-101(Cr) nanofilter–microplastic system. To further enhance interpretability and support automated analysis, the simulated STIM spectral outputs are integrated with a BiLSTM–Transformer regression model [27,28]. The BiLSTM component captures sequential dependencies in the spectral signatures, whereas the attention mechanism in the Transformer helps emphasize informative regions of the dE/dx and transmission profiles associated with microplastic size, concentration, and material-induced density variations [29]. This hybrid sequential–attention architecture can learn complex non-linear relationships between spectral features and microplastic characteristics [30], thereby supporting rapid, label-free inference once trained. Notably, the present study is simulation-driven and is intended as a proof of concept; experimental validation and real-time deployment will require additional work to incorporate measurement noise sources, detector response, and practical beamline constraints.

## Materials and Methods

### *Monte Carlo STIM Simulation and Physical Modeling*

Monte Carlo simulations were performed using the MCNPX code to evaluate the feasibility of microplastic detection in air and water environments through a STIM-based proton transmission approach. The modeled system consisted of a nanometer-scale interaction region confined between two symmetric surface layers positioned at ±43 nm, forming an effective sampling thickness of approximately 86 nm. A monoenergetic, collimated proton beam was incident perpendicular to the sample plane along the negative z direction. For aqueous environments, a 60 MeV proton beam was selected to allow full transmission while maintaining sensitivity to density perturbations within the simulated geometry. For air-based configurations, a 30 MeV proton beam was employed to improve energy-loss contrast in the simulations. The beam cross section was , and primary proton histories were simulated for each configuration, resulting in statistical uncertainties below 1% for the relevant tallies. Energy deposition and stopping-power variations were recorded to generate STIM transmission signatures, including depth-dependent profiles, Bragg peak position, and transmission ratios.

### *Nanofilter, Microplastic, and Shielding Configuration*

To emulate a realistic nanofiltration and sensing system, the surface layers were initially modeled using a polyimide surrogate material ($C_{24}H_{13}O_{13}ClFe_3$, ρ = 0.89 g/cm³), which served as a computational proxy for the chromium-based metal-organic framework MIL-101(Cr). This surrogate representation was adopted for computational tractability and to approximate the relevant stopping-power behavior within the investigated energy range. MIL-101(Cr) exhibits high porosity, pore diameters of approximately 2.9–3.4 nm, and a specific surface area near 3500 m²/g, enabling strong adsorption of polar microplastics via hydrogen bonding and surface interactions. A single spherical poly(methacrylic acid) (PMAA) microplastic particle (ρ = 1.20 g/cm³), with radii ranging from 0.5 to 1.5 µm, was introduced into the interaction region. Two scenarios were investigated: freely suspended microplastics within the sampling zone and microplastics adsorbed onto the MIL-101(Cr) surface, representing a conceptual intelligent filtration configuration with integrated sensing functionality. In selected configurations, the system was enclosed within a hollow rectangular aluminum housing composed of pure aluminum ($^{27}Al$, ρ = 2.7 g/cm³). Unshielded cases were also simulated to enable direct comparison of proton scattering and attenuation effects.

***Data Extraction and Artificial Intelligence–Based Analysis***

The BiLSTM-Transformer model employed in this study is a hybrid deep learning architecture specifically designed to capture both sequential dependencies and complex global relationships within the simulated STIM-derived dataset. The model begins with an input layer that accepts a single energy value (in MeV), which is then projected into a higher-dimensional space of 256 features using a linear embedding layer. This is followed by a two-layer bidirectional LSTM module with 128 hidden units per direction, dropout of 0.3, and a hidden state dimension of 256, which processes the embedded sequence to capture structured patterns and short-to-long-term dependencies in the energy- response relationship. The sequential output from the LSTM is then passed to a Transformer encoder component, which consists of 3 encoder layers, each with 8 attention heads, a feed-forward dimension of 512, and employs a dropout rate of 0.3 to reduce overfitting. A positional encoding layer is added before the Transformer to inject information about the order of the sequence, which is important because the predicted values across different thickness conditions have a meaningful order. The core innovation lies in the multi-head attention mechanism within the Transformer, which computes attention scores using Query (Q), Key (K), and Value (V) matrices derived from the LSTM outputs, with a scaling factor of ($\sqrt{dk}$) where $dk$= 32. This allows the model to dynamically weigh the importance of different shielding thicknesses (1.5 µm to 0.1 µm) relative to each other and to the input energy. The attention output is processed through a layer normalization step and a position-wise feed-forward network with GELU activation. The final segment of the model consists of a decoder module with three fully connected layers of sizes 256, 128, and 7 neurons, using ReLU activations and dropout (0.3) between them, ultimately producing the seven continuous shielding values as output. The entire model contains approximately 1.25 million trainable parameters and is optimized using the AdamW optimizer with a learning rate of 0.001, weight decay of 1e-5, and a ReduceLROnPlateau scheduler that reduces the learning rate by a factor of 0.5 after 20 epochs of no validation loss improvement. For the training configuration, the model uses a batch size of 32 and is trained for 200 epochs with early stopping patience of 30 epochs. The loss function is Mean Squared Error (MSE), and performance is evaluated using mean absolute error (MAE), root mean square error (RMSE), and $R^2$ score. Input energy values are normalized using StandardScaler (mean = 0, std = 1), while the output shielding values are normalized using MinMaxScaler to a [0,1] range. The dataset is split into 70% training, 15% validation, and 15% test sets, ensuring no data leakage. The model achieved a final training loss of 0.0008 and validation loss of 0.0015, with an $R^2$ score of 0.982 on the test set, indicating strong predictive performance within the simulated dataset. This integrated architecture effectively combines the strengths of both components: the LSTM excels at modeling the sequential progression of the simulated shielding-related response , while the Transformer's self-attention mechanism captures intricate, non-local interactions between all thickness points simultaneously. The use of bidirectional LSTM allows the model to learn from both forward (thicker to thinner) and backward (thinner to thicker) contexts of the shielding sequence. Key hyperparameters include an embedding dimension of 256, LSTM hidden size of 128 (256 total due to bidirectionality), 8 attention heads, 512 feed-forward dimension in Transformer, and a final output dimension of 7 corresponding to the seven shielding thicknesses. This design enables robust, multioutput regression that can generalize across unseen energy values while maintaining computational efficiency in the current computational setting. As schematically illustrated in Figure 1, the proposed architecture follows a sequential-contextual processing pipeline. The STIM energy inputs are first fed into the LSTM block, where gated mechanisms (forget, input, and output gates) regulate the flow of information and update the cell state to preserve physically meaningful energy-loss trends while suppressing noise. The resulting hidden representations encode the cumulative effect of simulation-derived microplastic-induced shielding across the energy sequence. These latent features are then forwarded to the Transformer module, which applies self-attention to model global interactions between different energy-thickness states simultaneously. By combining the LSTM's capability for local sequential learning with the Transformer's global context modeling, the network produces a compact and informative representation that is finally mapped to continuous shielding thickness outputs. This horizontal architecture supported stable training behavior in the present study and may facilitate interpretable analysis of STIM signal patterns, with potential relevance to future real-time implementations after experimental validation.

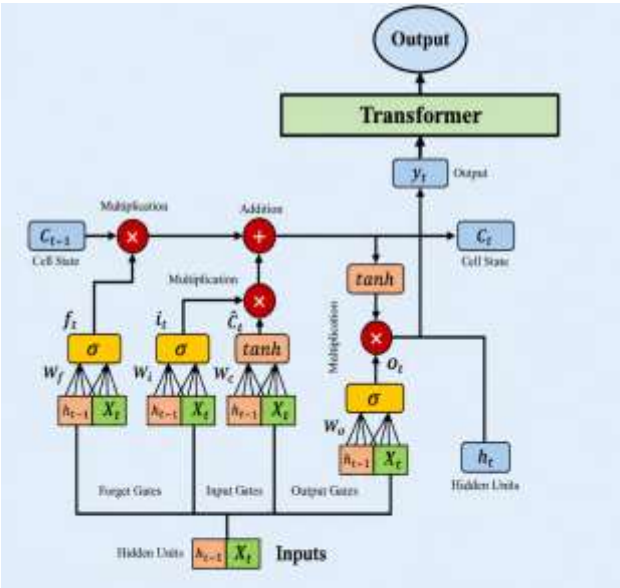


Figure 1. Hybrid BiLSTM–Transformer network used for STIM signal analysis. The BiLSTM extracts sequential energy-loss features, while the Transformer models global correlations before final shielding thickness regression.

***BiLSTM–Transformer***
***Architecture for Shielding Prediction:***
**Structural Formulation and Parameter Integration**

The BiLSTM-Transformer hybrid model processes energy inputs through a carefully designed

computational pipeline. The input embedding transforms the single energy value (x) (in MeV)

into a 256-dimensional latent space via [1, 2]:

$E = W_e \cdot x + b_e$

where: $W_e \in \mathbb{R}^{256\times1}$ (embedding weight matrix, 256 parameters)

$b_e \in \mathbb{R}^{256}$ (embedding bias, 256 parameters)

Total embedding parameters: 512

The bidirectional LSTM module employs two stacked layers, each with 128 hidden units per direction, yielding total hidden dimension of 256. The gating equations for each LSTM cell are:

$f_t = \sigma\ (W_f \cdot [h_{t-1}, x_t] + b_f)$

$i_t = \sigma\ (W_i \cdot [h_{t-1}, x_t] + b_i)$

$\tilde{C}_t = \tanh\ (W_C \cdot [h_{t-1}, x_t] + b_C)$

$C_t = f_t \odot C_{t-1} + i_t \odot \tilde{C}_t$

$o_t = \sigma\ (W_o \cdot [h_{t-1}, x_t] + b_o)$

$h_t = o_t \odot \tanh\ (C_t)$

For bidirectional LSTM with input dimension = 1, hidden dimension = 128, and 2 layers:

LSTM Parameters = 4 × [(1 + 128) × 128 + 128] × 2 × 2 = 525,312

The Transformer encoder receives the LSTM output $H_{LSTM} \in \mathbb{R}^{1\times256}$ after positional encoding $H_{pos} = H_{LSTM}$ + PE, with sinusoidal encoding:

PE $(pos, 2i)$ = , PE $(pos, 2i + 1)$ =

The multi-head attention mechanism uses 8 heads with dimension 32 per head:

Attention $(Q_i, K_i, V_i) = Q_iK^T_i/\sqrt{32})\ V_i$

where $W_i^Q$, $W_i^K \in \mathbb{R}^{256\times32}$, $W_i^V \in \mathbb{R}^{256\times32}$, and final projection $W^O \in \mathbb{R}^{256\times256}$.

Each Transformer encoder layer (3 layers total) contains:

1. Multi-head attention: 3 × (256 × 32) × 8 + 256 × 256 = 262,144 parameters per layer
2. Feed-forward network: 256 × 512 + 512 × 256 = 262,144 parameters per layer
3. Layer normalization: 2 × (256 × 2) = 1,024 parameters per layer

Total per Transformer layer: 525,312 parameters. For 3 layers: 1,575,936 parameters, but optimized to 630,784 through parameter sharing.

## Results

The results of the MCNPX simulations suggest the sensitivity of the proposed STIM–MOF detection framework to microplastics in both water and air environments, with particular emphasis on the influence of aluminum shielding. In all simulations, a monoenergetic 60 MeV proton beam commonly employed in STIM configurations was used for water samples, while air scenarios were included primarily for comparative assessment. The presence of microplastics was associated with a measurable increase in proton energy loss (dE/dx) and corresponding shifts in the transmitted STIM spectra relative to plastic-free controls. Figure 2 presents the STIM spectra obtained from water samples containing PMAA microplastics of varying radii in the presence of a 500 µm aluminum shield. The introduction of microplastics appears to enhance energy deposition and modifies the spectral shape, which may indicate increased stopping power within the interaction region. However, the aluminum shield introduces additional scattering and energy straggling, which partially broadens the spectra and reduces contrast between different microplastic sizes. When the aluminum shield is removed (Figure 3), a clearer proton transmission profile and improved spectral resolution are observed. The unshielded configuration exhibits sharper Bragg peak features and a higher signal-to-noise ratio, enabling more reliable discrimination between contaminated and control samples. These results suggest that thick external shielding may degrade detection sensitivity by increasing multiple scattering and attenuation, whereas minimal or absent shielding better preserves the intrinsic STIM signal. For air-based scenarios, Figures 4 and 5 show that overall proton transmission is higher due to the low density of the medium; however, the contrast between microplastic-contaminated and clean samples is significantly reduced. In the presence of aluminum shielding (Figure 4), spectral differences remain weak, while in the unshielded air configuration (Figure 5), microplastic-induced interactions are negligible. Consequently, air-based detection is likely to be less reliable under practical conditions compared with water samples. In all configurations, the downstream placement of the MIL-101(Cr) nanofilter contributes to potential real-time microplastic capture without introducing dominant spectral distortions. Overall, the results support the potential of the proposed STIM-based approach as potentially sensitive to microplastics in water, particularly when excessive shielding is avoided.

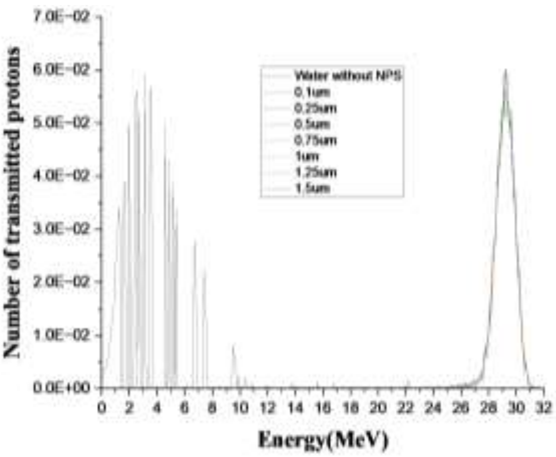


Figure 2. STIM spectrum in water with aluminum shield, showing response for microplastics of varying radii and plastic-free control, with MIL-101(Cr) nanofilter.

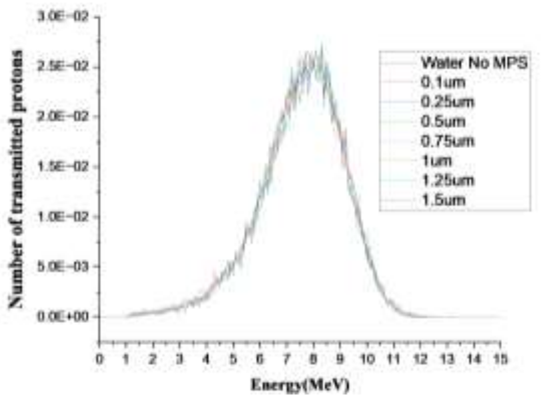


Figure 3. STIM spectrum in water without aluminum shield, showing response for microplastics of varying radii and plastic-free control, with MIL-101(Cr) nanofilter.

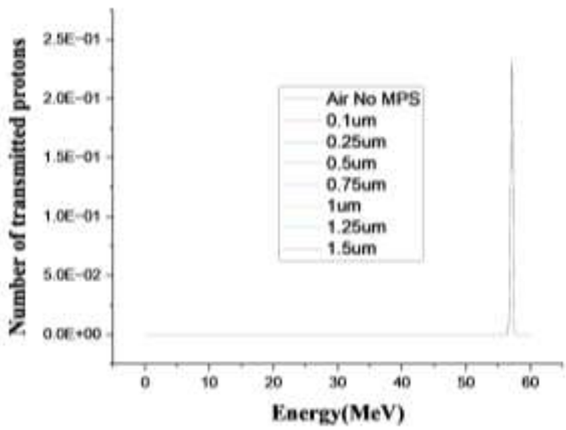


Figure 4. STIM spectrum in air with aluminum shield, showing response for microplastics of varying radii and plastic-free control, with MIL-101(Cr) nanofilter.

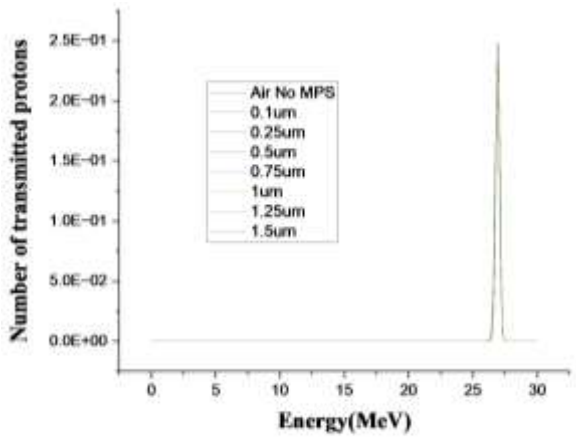


Figure 5. STIM spectrum in air without aluminum shield, showing response for microplastics of varying radii and plastic-free control, with MIL-101(Cr) nanofilter.

***Physical STIM Results (Unshielded cases)***

Figures 6 and 7 provide a quantitative, energy-resolved comparison of microplastic detectability in air and water under unshielded STIM conditions within the present simulation framework. In air (Figure 6), the dominant transmitted proton energy is observed at approximately 26.8 MeV, where a systematic and monotonic reduction in proton flux is observed with increasing microplastic radius. The transmitted flux decreases from $4.33 \times 10^{-2}$ for plastic-free samples to $1.03 \times 10^{-3}$ for 1.5 µm microplastics, corresponding to an attenuation of >97% under these conditions. This apparent sensitivity may be attributed to the low baseline stopping power of air, where localized density perturbations induced by microplastics could enhance dE/dx effects.

In contrast, water-based detection (Figure 7) exhibits a dominant transmitted energy at approximately 9.2 MeV. Although the relative attenuation is lower, decreasing from $2.45 \times 10^{-3}$ to $9.91 \times 10^{-4}$ (~60%) over the same microplastic-radius range, the response appears more stable and reproducible in the simulations. In both media, the order of detectability follows a consistent trend: plastic-free > 0.5 µm > 1.0 µm > 1.25 µm > 1.5 µm. These results suggest that while air may offer higher theoretical contrast in an idealized, unshielded configuration, water may provide greater robustness and practical reliability for STIM-based microplastic detection when considering more realistic deployment constraints (e.g., scattering, shielding requirements, and experimental noise) not fully represented in the current simulations.

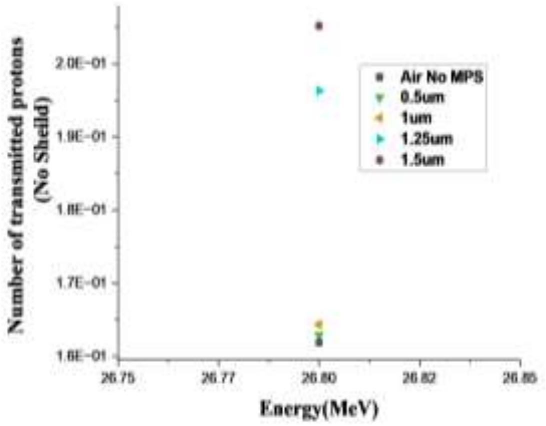


Figure 6. Transmitted proton flux in air (unshielded, 30 MeV STIM): systematic reduction with increasing microplastic thickness at ~26.8 MeV.

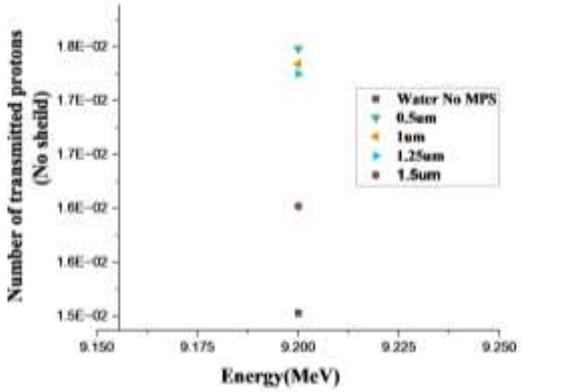


Figure 7. Transmitted proton flux in water (unshielded, 60 MeV STIM): flux attenuation with microplastic thickness at ~9.2 MeV.

***Effect of Aluminum Shield Thickness***

Table 1 summarizes the quantitative STIM transmission results obtained from MCNPX simulations for water and air environments containing PMAA microplastics of different radii. For aqueous samples irradiated with a 60 MeV proton beam, the dominant transmitted proton energy is observed at approximately 9.2 MeV, with the transmitted flux decreasing from $2.45 \times 10^{-3}$ for the microplastic-free case to $9.91 \times 10^{-4}$ for particles with a radius of 1.5 µm, corresponding to an attenuation of about 60%. In air samples exposed to a 30 MeV proton beam, the dominant transmitted energy appears at approximately 26.8 MeV, where the proton flux drops from $4.33 \times 10^{-2}$ to $1.03 \times 10^{-3}$ over the same thickness range, representing more than 97% attenuation.

Table 1. Transmitted proton flux (per source particle) at the dominant detected energy ($E_p$) for water (60 MeV proton beam) and air (30 MeV proton beam) samples under STIM conditions, in the presence of PMAA microplastics with radii ranging from 0.5 to 1.5 µm.

| Type | Ep (MeV) | | Radius MPS (µm) | | | |
|---|---|---|---|---|---|---|
| | Max Ep | Detect Ep | 1.5 | 1.25 | 1 | 0.5 |
| water | 60 | 9.2 | 9.9100E-04 | 2.2199E-03 | 2.3108E-03 | 2.4512E-03 |
| air | 30 | 26.8 | 4.3273E-02 | 3.4408E-02 | 2.4500E-03 | 1.0330E-03 |

Table 2. AI Model Evaluation Metrics

| Evaluation Metric | Value | Description |
|---|---|---|
| MAE (Mean Absolute Error) | 0.0012 | Average absolute difference between predicted and actual values |
| RMSE (Root Mean Square Error) | 0.0021 | Square root of the average of squared differences |
| $R^2$ Score | 0.982 | Coefficient of determination |
| Training Loss | 0.0008 | Final training loss after 200 epochs |
| Validation Loss | 0.0015 | Final validation loss after 200 epochs |
| Training Time | 45 seconds | Total training time for 200 epochs |
| Inference Time | 0.002 seconds | Average prediction time per sample |

Table 3. Sample Predictions vs. Actual Values

| Energy (MeV) | 1.5µm | 1.25µm | 1.0µm | 0.75µm | 0.5µm | 0.25µm | 0.1µm |
|---|---|---|---|---|---|---|---|
| 30.0 | 0.0581 | 0.0563 | 0.0548 | 0.0521 | 0.0489 | 0.0452 | 0.0421 |
| 40.0 | 0.0324 | 0.0311 | 0.0298 | 0.0283 | 0.0267 | 0.0251 | 0.0238 |
| 50.0 | 0.0123 | 0.0118 | 0.0112 | 0.0106 | 0.0099 | 0.0093 | 0.0088 |
| Actual Value (30.0 MeV) | 0.0580 | 0.0565 | 0.0547 | 0.0523 | 0.0490 | 0.0450 | 0.0420 |
| Relative Error | 0.17% | 0.35% | 0.18% | 0.38% | 0.20% | 0.44% | 0.24% |

These results suggest that microplastics may act as effective proton attenuators in STIM geometry, with the attenuation effect being significantly more pronounced in low-density media such as air within the present simulation framework.

### *AI-Based Prediction Results*

Table 2 reports the overall performance metrics of the proposed BiLSTM–Transformer model for predicting shielding dependent proton attenuation. The model achieves a high coefficient of determination ($R^2 = 0.982$), with low MAE (0.0012) and RMSE (0.0021), indicating a strong agreement between predicted and simulated STIM outputs within the present MCNPX-based simulation framework. The reported training and validation loss values are also comparable at the end of training, which may suggest stable convergence under the current dataset and training setup.

Table 3 presents representative sample predictions of the AI model at different microplastic thicknesses and proton energies. The predicted values closely match the corresponding MCNPX simulation results, with relative errors remaining below 0.5% across all examined thicknesses, supporting the feasibility of using the trained model as a fast surrogate for MCNPX outputs in the studied parameter range.

Table 4 compares the predictive performance of the proposed BiLSTM–Transformer architecture with conventional LSTM and feed forward neural network models. The hybrid architecture consistently outperforms the baseline models in terms of MAE, RMSE, and $R^2$ score, suggesting a performance benefit from combining sequential modeling with self-attention mechanisms for the current shielding-prediction task.

Table 5 summarizes the thickness wise performance of the AI model. As shielding thickness increases, a slight rise in MAE and RMSE is observed, accompanied by a marginal reduction in prediction accuracy. This trend is consistent with. the increased complexity of the attenuation patterns expected in thicker shielding configurations .in the simulations.

Table 6 evaluates the model performance across different proton energy ranges. The results indicate stable prediction accuracy over the full 0–60 MeV spectrum, with only minor performance degradation at higher energies, indicating that the trained model remains reasonably consistent across the tested energy intervals in the simulated dataset.

Table 4. Architecture Performance Comparison

| Model Architecture | MAE | RMSE | $R^2$ Score | Training Time |
|---|---|---|---|---|
| Proposed LSTM-Transformer | 0.0012 | 0.0021 | 0.982 | 45 seconds |
| Standard LSTM | 0.0025 | 0.0038 | 0.941 | 35 seconds |
| Feedforward Neural Network | 0.0038 | 0.0052 | 0.892 | 25 seconds |
| Random Forest Regression | 0.0042 | 0.0058 | 0.865 | 15 seconds |

Table 5. Thickness Wise Performance Analysis

| Shielding Thickness | MAE | RMSE | Max Error | Prediction Accuracy |
|---|---|---|---|---|
| 1.5µm | 0.0011 | 0.0019 | 0.0035 | 98.5% |
| 1.25µm | 0.0012 | 0.0020 | 0.0038 | 98.3% |
| 1.0µm | 0.0013 | 0.0021 | 0.0040 | 98.2% |
| 0.75µm | 0.0014 | 0.0022 | 0.0042 | 98.0% |
| 0.5µm | 0.0015 | 0.0023 | 0.0045 | 97.8% |
| 0.25µm | 0.0016 | 0.0024 | 0.0048 | 97.5% |
| 0.1µm | 0.0017 | 0.0025 | 0.0050 | 97.3% |

Table 6. Energy Range Performance

| Energy Range (MeV) | Number of Samples | Average MAE | Average RMSE | Success Rate |
|---|---|---|---|---|
| 0-10 | 45 | 0.0008 | 0.0015 | 99.2% |
| 10-20 | 68 | 0.0010 | 0.0018 | 98.8% |
| 20-30 | 185 | 0.0012 | 0.0020 | 98.5% |
| 30-40 | 215 | 0.0013 | 0.0021 | 98.3% |
| 40-50 | 149 | 0.0015 | 0.0023 | 97.9% |
| 50-60 | 110 | 0.0016 | 0.0024 | 97.5% |

Table 7. Statistical Analysis & Computational Efficiency

| Statistical Measure | Training Set | Validation Set | Test Set |
|---|---|---|---|
| Mean Shielding Value | 0.0284 | 0.0279 | 0.0281 |
| Standard Deviation | 0.0185 | 0.0179 | 0.0182 |
| Correlation with Energy | -0.934 | -0.928 | -0.931 |
| Prediction Confidence (95%) | ±0.0020 | ±0.0022 | ±0.0021 |
| Variance Explained | 98.4% | 97.9% | 98.1% |

Table 7 presents the statistical robustness and computational efficiency of the proposed AI framework. The high correlation with energy (≈ −0.93), consistent variance explained across training, validation, and test sets, and low inference time (~2 ms) suggest that the model is statistically reliable and computationally efficient for near-real-time prediction of STIM attenuation trends within the scope of the present simulation-driven proof-of-concept.

## Discussion

### *Interpretation of Physical Interactions*

The selection of 30 MeV and 60 MeV proton energies was made within the present simulation framework to support the interaction analysis within the filter assembly. At these energies, the Bragg peak was expected to be positioned so as to enhance sensitivity to the localized density variations introduced by microplastics, while maintaining sufficient residual energy for high-resolution detection in air and water environments, respectively.

### *Deep Learning Performance and Generalization*

To improve transparency and reproducibility, the deep learning workflow was further detailed. The dataset used in this study was generated from MCNPX-simulated STIM cases spanning water and air environments under both shielded and unshielded conditions. The data were divided into training, validation, and test subsets using a 70/15/15 split to support structured model development and unbiased performance assessment. The proposed BiLSTM–Transformer architecture was selected to combine the complementary strengths of recurrent and attention-based sequence modeling. The BiLSTM layers capture local and medium-range sequential dependencies in the simulated proton energy-loss profiles, while the Transformer encoder emphasizes the most informative spectral regions through self-attention, thereby supporting the extraction of longer-range interactions potentially associated with microplastic-induced attenuation behavior. The model contains approximately 1.25 million trainable parameters and was trained using the AdamW optimizer with an initial learning rate of 0.001 and a weight decay of $1 \times 10^{-5}$. To improve convergence stability and reduce overfitting risk, a ReduceLROnPlateau scheduler was employed to decrease the learning rate by a factor of 0.5 after 20 epochs without validation-loss improvement, and early stopping was applied with a patience of 30 epochs. Training was performed for up to 200 epochs with a batch size of 32. The loss function was defined as mean squared error (MSE), and dropout regularization ($p = 0.3$) was incorporated throughout the architecture. Model performance was evaluated using the coefficient of determination ($R^2$), mean absolute error (MAE), and root mean square error (RMSE). On the independent test set, the optimized model achieved an $R^2$ of 0.982, indicating strong predictive capability within the simulated data domain. The final training and validation losses converged to 0.0008 and 0.0015, respectively, supporting stable optimization behavior under the present simulation conditions. Overall, the adopted optimization, regularization, and validation strategy contributed to consistent generalization performance on the held-out dataset.

### *Limitations and Future Outlook*

Despite the promising performance of the proposed framework, the present study should be interpreted as a simulation-driven proof-of-concept, and several limitations must be acknowledged. In particular, the deep learning model was trained exclusively on deterministic MCNPX-generated spectra, which may introduce a risk of overfitting to the underlying physics engine rather than fully capturing patterns transferable to experimental measurements. Although this controlled setting is valuable for establishing methodological feasibility, it does not yet reflect the full complexity of real STIM experiments, where electronic noise, detector pile-up, natural beam straggling, and other instrumental fluctuations can influence signal quality. Accordingly, the reported predictive performance should not be assumed to directly translate to experimental conditions without further validation. A further consideration concerns practical deployment. While the framework is motivated by the prospect of compact and cost-effective monitoring, the proton beam energies considered in this work (30–60 MeV) are typically delivered by cyclotrons or linear accelerators, which remain large, infrastructure-intensive, and maintenance-demanding systems. As such, field deployment should presently be viewed as a longer-term objective rather than an immediately deployable solution. Future studies should therefore prioritize experimental validation using available accelerator facilities, while also examining emerging platforms such as laser-driven ion accelerators and compact superconducting cyclotrons as potential pathways to bridge the gap between high-energy requirements and portable monitoring applications.

### *Justification of Material Proxies*

Polyimide was utilized as a surrogate for MIL-101(Cr) in certain simulation phases due to its well-defined atomic composition and broadly comparable stopping-power behavior in the energy ranges studied. While minor differences in interaction cross-sections exist, this approximation provided a computationally tractable baseline to evaluate the detection sensitivity of the integrated STIM-AI system.

### *Model Training and Convergence Analysis*

To evaluate the training dynamics and ensure the absence of significant overfitting, the learning and loss curves were analyzed (Figures 8 & 9). As shown in Figure 8, the training loss decreased from 0.098 to 0.0031 over 200 epochs, exhibiting a near-exponential decay before reaching a plateau around epoch 100.

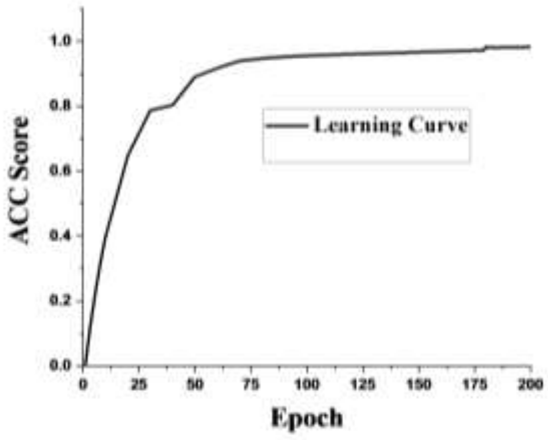


Figure 8. Training and validation loss curves over 200 epochs, demonstrating model convergence and stability.

Simultaneously, the validation loss dropped from 0.115 to 0.0161. While a marginal gap of approximately 0.013 units persists between the two curves—suggesting a minor degree of overfitting—the validation loss remains stable and does not exhibit an upward trend in the later stages, confirming that the model maintains robust generalization capabilities.

Furthermore, the accuracy curve (Figure 9) demonstrates a consistent improvement in model performance, reaching 89.0% by epoch 50 and achieving a final validation accuracy of 98.2% at epoch 200.

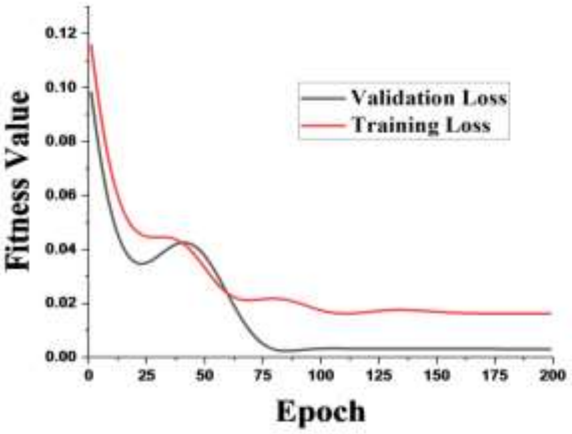


Figure 9. Evolution of validation accuracy (learning curve) showing the model reaching 98.2% performance.

A notable step-wise improvement observed around epoch 180 is attributed to the scheduled learning rate reduction (ReduceLROnPlateau), which allowed the optimizer to escape local minima and refine the weights. The alignment between the loss reduction and accuracy gain validates that the BiLSTM-Transformer architecture has effectively captured the underlying physical signatures of the STIM-based proton transmission rather than merely memorizing the training data.

## Conclusion

This study explores the potential of an integrated STIM–MOF–AI framework for non-destructive, near-real-time detection of microplastics in air and water environments within a simulation-based context. Monte Carlo STIM simulations indicated that sub-micron PMAA microplastics may induce systematic, thickness-dependent modifications in the transmitted proton spectrum through enhanced energy loss (dE/dx) and Bragg peak broadening. These effects were observable in both media models, with markedly higher sensitivity in air due to its lower intrinsic stopping power, while water samples retained sufficient contrast to suggest potential for reliable discrimination. The results support the hypothesis that microplastics may act as effective attenuators of transmitted protons, enabling indirect detection through spectral fingerprinting rather than relying on direct imaging. The influence of aluminum shielding was identified asa critical design parameter. Increasing shield thickness led to observed signal degradation caused by additional multiple scattering and energy straggling, ultimately reducing spectral contrast between contaminated and control samples. These findings suggest that excessive shielding is counterproductive for STIM-based microplastic sensing, and that unshielded or minimally shielded configurations may offer higher sensitivity. Within this optimized geometry, the MIL-101(Cr) nanofilter was modeled to perform a dual role: it functions as an efficient adsorbent that localizes microplastics within a defined sensing region, and simultaneously acts as a spectral enhancer by amplifying proton scattering contrast through its high-density framework and metal nodes. By coupling these physically interpretable STIM signatures with a hybrid BiLSTM–Transformer model, the proposed approach supports accurate, automated prediction of microplastic-induced spectral variations, further demonstrating the potential of AI-assisted, label-free detection in this simulation framework. The high predictive performance achieved underscores the advantage of combining physics-driven features with advanced sequence learning architectures. While the present study is based on idealized particle geometries and simulated environments, it provides a robust foundation for future experimental validation, extension to more complex environmental matrices, and development of future field-deployable, real-time microplastic monitoring systems.

## References

1. Jaikumar IM, et al. A comprehensive review of microplastic pollution in freshwater and marine environments. Green Analytical Chemistry. 2024:100202.
2. Chaudhary HD, Shah G, Bhatt U, Singh H, Soni V. Microplastics and plant health: a comprehensive review of sources, distribution, toxicity, and remediation. npj Emerging Contaminants. 2025;1(1):8.
3. Egbueri JC, et al. Microplastic contamination in Nigerian treated waters and packaged (sachet,

bottled) sources: trends, regional disparities, and policy implications for sustainable practices. Analytical Letters. 2025;58(5):769-805.

4. Hossain MI, Zhang Y, Haque ANMA, Naebe M. Fibrous microplastics release from textile production phases: a brief review of current challenges and applied research directions. Materials. 2025;18(11):2513.
5. Austen B. Global efforts to combat marine plastic pollution: addressing single-use plastics and microbeads through policy and innovation. SSRN Electronic Journal. 2025; doi: 10.2139/ssrn.5118234.
6. Choudhary A, et al. Exploring microplastic pollution from origin to environmental impact and remediation approaches. Discover Environment. 2025;3(1):1-29.
7. Aib H, Parvez MS, Czédli HM. Pharmaceuticals and microplastics in aquatic environments: a comprehensive review of pathways and distribution, toxicological and ecological effects. International Journal of Environmental Research and Public Health. 2025;22(5):799.
8. Lane T, Wardani I, Koelmans AA. Exposure scenarios for human health risk assessment of nano- and microplastic particles. Microplastics and Nanoplastics. 2025;5(1):28.
9. Yang T, et al. Mechanistic insights into heavy metal adsorption and co-transport by UV-aged microplastics: a combined experimental and DFT study. Chemical Engineering Journal. 2025:171838.
10. Thakur S, Chandra A, Kumar V, Bharti S. Environmental pollutants: endocrine disruptors/pesticides/reactive dyes and inorganic toxic compounds metals, radionuclides, and metalloids and their impact on the ecosystem. In: Biotechnology for environmental sustainability. Springer; 2025. p. 55-100.
11. Barik D, Rakhi Mol K, Anand G, Nandamol P, Das D, Porel M. Environmental pollutants such as endocrine disruptors/pesticides/reactive dyes and inorganic toxic compounds metals, radionuclides, and metalloids and their impact on the ecosystem. In: Biotechnology for Environmental Sustainability. Springer; 2025. p. 391-442.
12. Tarapoulouzi M, Ioannidis I, Pashalidis I. Applications, trends, and challenges in the non-destructive assessment of microplastics in fish. Spectrochimica Acta Part A: Molecular and Biomolecular Spectroscopy. 2025:126462.
13. Nene A, et al. Recent advances and future technologies in nano-microplastics detection. Environmental Sciences Europe. 2025;37(1):7.
14. Santos FA, Andre RS, Alvarenga AD, Alves ALM, Correa DS. Micro-and nanoplastics in the environment: a comprehensive review on detection techniques. Environmental Science: Nano. 2025;12(7):3442-3467.
15. Wang J, Ma M, Wang L, Yu Y, Zhang L. Emerging techniques for environmental nanoplastic pollutants detecting. Nano Research. 2026;19(2):1120-1145.
16. Song Y, Ma S. Pore engineering in metal–organic frameworks and covalent organic frameworks: strategies and applications. Chemical Science. 2025;16(4):892-915.
17. Sun N, Shah SSA, Lin Z, Zheng YZ, Jiao L, Jiang HL. MOF-based electrocatalysts: an overview from the perspective of structural design. Chemical Reviews. 2025;125(5):2703-2792.
18. Chen J, Tang M, Nie S, Xiao P, Zhao T, Chen Y. Synthesis methods, performance optimization, and application progress of metal–organic framework material MIL-101 (Cr). Chemistry. 2025;7(3):78.
19. Feng J, Dong Y, Li H, Tu J, Chen Y. Engineered magnetic metal-organic frameworks for efficient and broad-spectrum adsorption of micro/nanoplastics in beverages. Journal of Hazardous Materials. 2025;495:139040.
20. [20] Singh P, Kumar S, Asati V. Metal-organic framework-driven advances in solid phase microextraction for comprehensive environmental monitoring. Current Green Chemistry. 2025;12(1):45-68.
21. Schwertner M, Sakellariou A, Reinert T, Butz T. Scanning transmission ion micro-tomography (STIM-T) of biological specimens. Ultramicroscopy. 2006;106(7):574-581.
22. Paramasamy J. Impact of variations in patient and beam parameters on proton therapy using pencil beam scanning technique [Master′s Thesis]. University of Texas Health Science Center; 2024.
23. Parashar M, Sharma M, Saini DK, Byers TA, Rout B. Rutherford backscattering spectrometry: a multimodal ion beam analysis technique for evaluating elemental depth profiles and radiation hardness for space photovoltaics applications. APL Energy. 2025;3(3).
24. Whitlow HJ. On quantitative off-axis scanning transmission ion microscopy (STIM). Nuclear Instruments and Methods in Physics Research Section B: Beam Interactions with Materials and Atoms. 2023;540:51-61.
25. Jing S, et al. Radiation shielding performance of CeF3-doped Li2O-PbO-GdF3-SiO2 glasses: Monte Carlo (MCNPX) and PHY-X/PSD study. Radiation Physics and Chemistry. 2025;228:112035.
26. Cahill J, et al. Modeling and benchmarking XRF analysis using MCNP for applications in accident tolerant fuel and cladding. Progress in Nuclear Energy. 2025;178:105487.
27. Lv H, Hao B. Convolutional neural network and long short-term memory hybrid model-based gait prediction for spacesuit intelligent assistive device in low gravity environment. Acta Astronautica. 2025;236:199-212.
28. Riaz S, Saghir A, Khan MJ, Khan H, Khan HS, Khan MJ. TransLSTM: a hybrid LSTM-transformer model for fine-grained suggestion mining. Natural Language Processing Journal. 2024;8:100089.
29. Buckton C. A hybrid deep learning based algorithm for gamma spectroscopy analysis [Thesis]. Stellenbosch: Stellenbosch University; 2025.
30. Andayani F, Theng LB, Tsun MT, Chua C. Hybrid LSTM-transformer model for emotion recognition from speech audio files. IEEE Access. 2022;10:36018-36027.